Chapter 11
Defects on Strontium Titanate

Matthew S.J. Marshall, Andres E. Becerra-Toledo, Laurence D. Marks and Martin R. Castell

Abstract Transition metal oxides sharing the perovskite structure exhibit many scientifically interesting and technologically important phenomena, and defects in these materials play a critical role in determining their properties. In the most general sense, $SrTiO_3$ is a suitable model system for the study of defects in perovskite oxide materials. This chapter reviews common surface and defect structures in $SrTiO_3$, and concludes with a discussion of defect diffusion.

11.1 Introduction

Transition metal oxides sharing the perovskite oxide structure (ABO_3) exhibit nearly all of the most interesting phenomena in condensed matter physics including superconductivity, ferroelectricity and magnetism. $SrTiO_3$ is the archetypal perovskite oxide, it is both among the most widely studied members of this class of materials and is also commonly used as a substrate for thin film growth of other oxides. It has emerged that defects in $SrTiO_3$ give rise to several important properties, including blue light emission [1], localized conductivity [2], and electron doping [3]. A comprehensive review of defects in $SrTiO_3$ is therefore useful in

M.S.J. Marshall
Department of Applied Physics, Yale University, 15 Prospect St. Becton Center, New Haven, CT 06510, USA

M.S.J. Marshall
Center for Research on Interface Structures and Phenomena (CRISP), Yale University, New Haven, CT 06510, USA

A.E. Becerra-Toledo · L.D. Marks
Department of Materials Science and Engineering, Northwestern University, Evanston, IL 60208, USA

M.R. Castell (✉)
Department of Materials, University of Oxford, Parks Road, Oxford OX1 3PH, UK
e-mail: martin.castell@materials.ox.ac.uk

J. Jupille and G. Thornton (eds.), *Defects at Oxide Surfaces*,
Springer Series in Surface Sciences 58, DOI 10.1007/978-3-319-14367-5_11

elucidating the origin of the properties of this prototypical oxide, and is of general utility in informing future studies of defects in other perovskite oxide systems.

Understanding defect diffusion and defect structure are important when considering the various technological applications of $SrTiO_3$. For instance, easily reducible oxides such as $SrTiO_3$ must be treated carefully if they are to be used as dielectric materials [4], because oxygen deficiency gives rise to electrical conductivity. Moreover, the operation of resistive memory devices that include $SrTiO_3$ [5] involve point and cluster defect diffusion over short time scales. Finally, doping and defect engineering is critical to oxide electronics, particularly for materials with low carrier concentrations such as $SrTiO_3$ [6].

$SrTiO_3$ is also of interest due to the formation of TiO_2-rich nanostructures that decorate its surface after vacuum annealing [7]. These nanostructures are useful templates for the deposition of atoms or molecules, and may also be of interest for catalysis. This chapter will begin with a discussion of bulk defects found in $SrTiO_3$, such as point defects and vacancy clusters, and how these relate to the properties of $SrTiO_3$. An understanding of surface defects necessitates a brief overview of the structure of the $SrTiO_3$ surface, followed by a review of recent advances in determining defect structures. Finally, we will conclude with a discussion of the diffusion of defects in $SrTiO_3$. While there has been excellent work on the (110) and (111) surfaces of $SrTiO_3$, for the sake of brevity, our focus is on the widely-studied (001) surface. Similarities can be found between the defective TiO_x structures encountered in the present chapter and those found in studies dedicated to titania surfaces (Chaps. 1–4, 14).

11.2 Defects in Bulk $SrTiO_3$

11.2.1 Point Defects

$SrTiO_3$ has both cation and anion point vacancies, as well as interstitial defects. The most widely studied defect in $SrTiO_3$ is the oxygen vacancy, which is known to render $SrTiO_3$ conductive at a carrier density of 10^{19} cm^{-3} [8]. First principles density functional theory (DFT) calculations also predict antiferrodistortive rotations of the oxygen octahedra to occur around oxygen vacancies [9]. In thin films of $SrTiO_3$ grown with pulsed laser deposition (PLD), Ti and Sr vacancies have been observed with positron annihilation spectroscopy [10], where the relative concentration of V_{Ti}/V_{Sr} was related to the laser fluence during growth. DFT calculations reveal that Ti antisitelike defects near strontium vacancies have a strong polar distortion [11]. The results of these calculations are shown in Fig. 11.1b, where a Ti atom, shown in dark blue, is substituted at the site of a Sr vacancy, shown as a black square. A bulk $SrTiO_3$ unit cell is shown for reference in Fig. 11.1a. The antisitelike Ti defect has stable polar configurations along the [100] and [110] directions, and has been proposed as the origin of ferroelectricity observed in thin films of Sr-deficient $SrTiO_3$ [12, 13]. We should also note that Schottky-like SrO vacancy

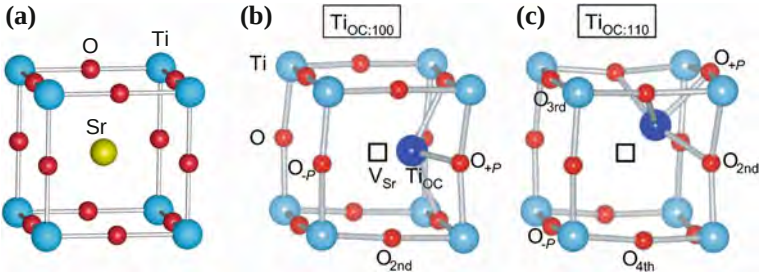

Fig. 11.1 **a** The stoichiometric $SrTiO_3$ unit cell. Ti antisitelike defect at the site of an Sr vacancy leads to a significant polar distortion of Ti along the **b** [100] and **c** [110] directions (Ti antisitelike defect = *dark blue*, Ti lattice = *light blue*, oxygen = *red*, Sr = *yellow*). V_{Sr} denotes a Sr vacancy and Ti_{OC} denotes an interstitial Ti atom at the site of the Sr vacancy. Reprinted figure adapted with permission from Choi et al. [11]. Copyright (2011) by the American Physical Society [11] (Color figure online)

pairs are predicted to have the lowest energy configuration of any point defect in $SrTiO_3$ [14]. There is a large and excellent body of work on point defects in $SrTiO_3$ and other oxides, e.g. in [15].

11.2.2 Vacancy Clusters

Studies of point defect clusters initially focused on oxygen vacancies. Analysis of transmission electron micrographs (TEM) of $SrTiO_3$ thin films indicated that oxygen vacancy clusters form in the as-grown thin film, which was a hitherto unexplored possibility [16]. DFT calculations revealed that clustering of oxygen vacancies into linear pairs is energetically favourable, as shown in Fig. 11.2, which

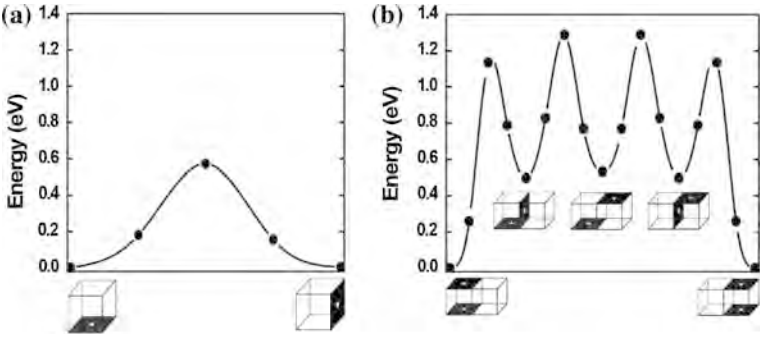

Fig. 11.2 **a** Total energy as a function of oxygen vacancy configuration for a single oxygen vacancy. **b** The energies of different configurations of oxygen divacancies, showing linear configurations of divacancies to have the lowest energy compared to alternative configurations. Reprinted figure with permission from Cuong et al. [17]. Copyright (2007) by the American Physical Society [17]

shows the total energy for different oxygen vacancy configurations [11]. These oxygen divacancies exhibit a stable linear configuration about a Ti atom, a configuration that may be generalisable to other perovskite oxides. Clustering of vacancies about Ti affects the electronic properties of the material by preferentially filling Ti *d*-orbitals with electrons [17]. Oxygen vacancies can be easily introduced into $SrTiO_3$ by annealing in vacuum and small amounts of excess Ti during the growth of $SrTiO_3$ can also cause clusters of strontium vacancies to form [18]. In addition to polar antisitelike defects, complexes of Sr and O vacancies have also been investigated as the potential origin of ferroelectricity in thin films [19]. To investigate the existence of these vacancy clusters, positron annihilation spectroscopy of homoepitaxial thin films grown using pulsed vapour deposition revealed a uniform distribution of Sr vacancies as well as large vacancy clusters in the near surface region [20]. The formation of vacancy clusters during thin film growth was attributed to Ti-poor films [10].

Annealing $SrTiO_3$(001) in reducing conditions results in a surface enriched with TiO_2 which upon extended annealing results in the growth of anatase TiO_2 islands [21, 22]. An oxidising anneal gives rise to secondary phases of SrO on the surface [23–25]. A number of models exist that attempt to explain this behaviour using a variety of arguments involving preferential surface segregation and sublimation behaviour. The most cohesive model is that by Meyer et al. [26] for donor doped $SrTiO_3$. At high temperatures electronic compensation of defects may be replaced by cation vacancy compensation in the form of Sr vacancies in the bulk. Because Schottky-type disorder is favoured in $SrTiO_3$, Sr vacancies are accompanied by the formation of Sr-rich phases at the surface [26], which are oxided and result in SrO islands.

11.2.3 Ruddlesden-Popper Phases

The Ruddlesden-Popper (RP) phases of $SrTiO_3$ have a $Sr_{n+1}Ti_nO_{3n+1}$ structure, first proposed by Ruddlesden and Popper [27, 28]. In its simplest form for n = 1 (Sr_2TiO_4), it corresponds to the removal of a TiO_2 layer from the perovskite $SrTiO_3$ structure resulting in a double-layer of SrO. Szot et al. annealed as-received crystals of $SrTiO_3$ in an oxidising atmosphere and found a SrO-rich surface with Ruddlesden-Popper phases in the bulk, while annealing in a reducing atmosphere results in TiO and TiO_x-rich surface phases [23, 29]. In bulk $SrTiO_3$, RP phases occur in oxidising conditions at high temperatures. One technological application of RP phases are as potential thermoelectric materials [30]. The RP phases of $SrTiO_3$ have also been grown in thin film form using molecular beam epitaxy [31, 32] and are predicted to have a variety of intriguing properties [33, 34].

11.2.4 Dislocations and Defects

In a naïve first approximation, reduction of $SrTiO_3$ is assumed to have a uniform character. However, as discussed in the preceding sections, a body of work has gradually emerged that demonstrates that oxygen vacancies tend to cluster, and that non-stoichiometric films of $SrTiO_3$ are subject to the formation of cation defects. While reduction of $SrTiO_3$ renders it conductive by doping with oxygen vacancies in the dilute limit, it has also been revealed that such reduction of $SrTiO_3$ can be inhomogeneous. For instance, high electronic conduction along dislocations leads to self-healing of the dislocation. This self-healing effect enhances oxygen vacancy mobility along dislocations, and as a result O vacancies tend to cluster along dislocations [35, 36]. Chemical etching of $SrTiO_3$ can reveal dislocations as shown in Fig. 11.3, where a tapping mode atomic force microscopy (AFM) image shows dislocations (black circles) clustered along distinct crystallographic directions. The technological relevance of this line of enquiry was demonstrated by Szot et al., who showed that clustering of oxygen vacancies along dislocations that are oriented along the crystallographic axes can be used to realise bistable nanowires that switch from insulating to metallic upon oxidation or reduction respectively [2].

11.2.5 Defects Introduced by Ar-Bombardment

Doping $SrTiO_3$ with oxygen vacancies reduces the crystal, and is often accomplished by annealing in vacuum. However, oxygen vacancies are also generated in $SrTiO_3$ by low-energy (<500 eV) bombardment with Ar-ions. Ion bombardment of $SrTiO_3$ led to the discovery of blue-light emission at room temperature [1], as well

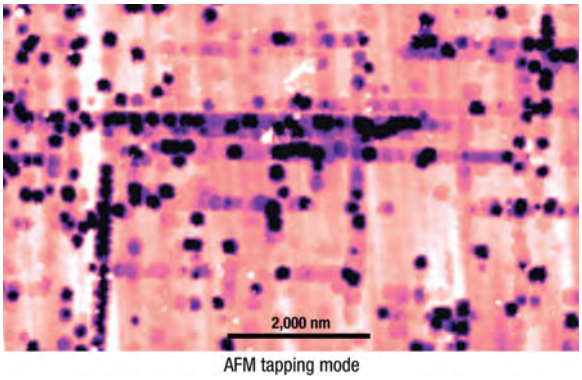

Fig. 11.3 A tapping mode AFM image of etch pits on $SrTiO_3$(001). *Purple* dislocations are aligned along crystallographic directions. Reprinted by permission from Macmillan Publishers Ltd. [2]. Copyright (2006) [2] (Color figure online)

as localized conductivity [37]. There are two advantages of introducing oxygen vacancies via low-energy ion bombardment versus reductive annealing. The first is that the distribution of vacancies can be spatially localized, because the depth of the oxygen vacancy profile is dependent on the penetration depth of the argon ions. The second advantage is that patterns can be easily created using widely available argon ion milling techniques. Blue light emission from Ar-ion bombarded $SrTiO_3$ was found to originate from electron doping that introduced defect states into the middle of the band gap, as shown in Fig. 11.4. Emission of blue light arises from the recombination of doped electrons in the conduction band and excited holes [38, 39].

The localized penetration depth is also consequential for creating transparent conducting $SrTiO_3$ that has a similar carrier density to $InSnO_3$ (ITO) [1] (see Chap. 11 for details on ITO). Transmission electron microscopy (TEM) images taken of $SrTiO_3$(001) single crystals following low-energy ion bombardment (<500 eV) reveal a 3 nm thick amorphous region atop a 20 nm thick region depleted of oxygen. This abrupt transition is shown in Fig. 11.5. The depth of argon ion impingement, or the ion penetration length, L, is given by [37]:

$$L = 1.1\frac{E^{2/3}W}{\rho\left(Z_i^{\frac{1}{4}} + Z_t^{\frac{1}{4}}\right)} \tag{11.1}$$

where E is the energy in eV, W is the atomic weight of the target in atomic mass units, ρ is the target density, and $Z_{i,t}$ are the atomic numbers of the ion and target respectively [37, 40]. For $SrTiO_3$, this simplifies to $L = 0.47\ E^{2/3}$, from which one can determine the depth of the amorphous layer to be 3 nm at an Ar ion energy of

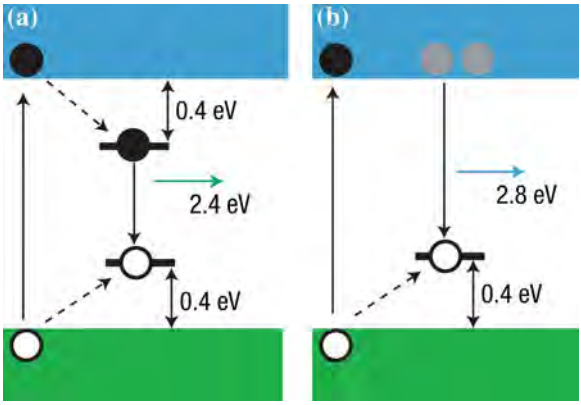

Fig. 11.4 **a** A schematic showing emission of *green light* at low temperatures and **b** *blue light* at room temperature from $SrTiO_3$. The *green rectangle* corresponds to the O 2*p* valence band while the *blue rectangle* corresponds to the Ti 3*d* conduction band. The *white circles* are holes, the *black circles* are electrons, and the *grey circles* are doped electrons. Reprinted by permission from Macmillan Publishers Ltd. [1]. Copyright (2005) [1] (Color figure online)

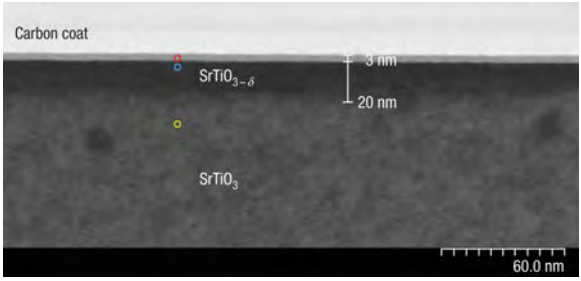

Fig. 11.5 A cross-sectional transmission electron micrograph (TEM) of $SrTiO_3(001)$ following bombardment by low-energy Ar^+ ions. A 3 nm thick amorphous layer is visible atop a darker 20 nm layer that is depleted of oxygen. Reprinted by permission from Macmillan Publishers Ltd. [1]. Copyright (2005) [1]

500 eV, in agreement with the experimentally measured values [1, 37]. Nonetheless, while the amorphous region is only a few nanometres thick, scattering deeper into the crystal generates oxygen vacancies up to a depth of an additional 20 nm, as shown in Fig. 11.5. This suggests preferential scattering between Ar and O, resulting in large numbers of oxygen vacancies.

11.3 Surfaces of $SrTiO_3$

11.3.1 Surface Structure of $SrTiO_3(001)$

To understand defects on the surface of $SrTiO_3$ necessitates an understanding of the surface structure. As such, this section will provide a brief overview of some important aspects surrounding the structure of $SrTiO_3$ surfaces. There exists a large and thorough body of work on the subject, and we would encourage the reader to further exploration of the literature [3, 10, 41–52]. The challenge of determining the structure of the $SrTiO_3$ surface requires a variety of techniques working in concert, in particular transmission electron microscopy (TEM), electron and X-ray diffraction, ultra high vacuum scanning tunnelling microscopy (UHV-STM), and first principles density functional theory (DFT). In general, surface reconstructions and surface phases of $SrTiO_3$ are terminated with TiO_2. Using electron diffraction and density functional theory, it was discovered that the structure of the (2×1) reconstruction consists of a double-layer termination of TiO_2 [44]. The stability of this model was evaluated by Johnston et al. who compared the double-layer TiO_2 structure to a proposed Ti_2O_3 structure [41, 43]. They found that under realistic experimental conditions, the double-layer TiO_2 model is most stable.

11.3.2 Polyhedral Quartet Structural Motif

An important milestone in elucidating the structure of $SrTiO_3(001)$ is the idea that different reconstructed or nanostructured surfaces share similar fundamental structural units. This first came about by using electron diffraction and DFT to solve the structure of the $c(4 \times 2)$ surface, finding that similar to other $SrTiO_3$ surfaces, it has a double-layer TiO_2 termination [45, 46]. More importantly, the top layer consists of a periodic pattern of a defining structural feature—four edge sharing TiO_5[] octahedra with "[]" a missing oxygen site, thus leading to the term 'polyhedral quartet motif.'

The structure of the polyhedral quartet motif is shown in a polyhedral representation of the $c(4 \times 2)$ surface in Fig. 11.6a, b and in a plan-view schematic in Fig. 11.6c. In Fig. 11.6c the black lines of the $c(4 \times 2)$ unit cell enclose a polyhedral quartet. STM images of the $c(4 \times 2)$ reconstruction are shown in Fig. 11.6d–f, and Auger electron spectroscopy (AES) demonstrated that the surface is rich in Ti [42]. At first glance, the structural model in Fig. 11.6a–c and the STM images in Fig. 11.6d–f look dramatically different, but the apparent difference was resolved using STM simulations derived using first principles calculations [53]. The simulations revealed that a single spot in the STM image is in fact comprised of four titanium atoms and eight oxygen atoms. The STM simulation is superimposed over an STM image of the $c(4 \times 2)$ surface Fig. 11.6g. Recent high resolution TEM and electron energy loss (EELS) spectroscopy offer further confirmation of the structure of the $c(4 \times 2)$ reconstruction [52].

While the $c(4 \times 2)$ is the first structure found with this quartet motif and has a four-member ring, as shown in Fig. 11.6a, others are now known from either, or both, experiment [48] or DFT calculations [46]. As shown in Fig. 11.7a, the (2×2) is a four-member zigzag linear arrangement along a [100] direction and the $(\sqrt{2} \times \sqrt{2})$ R45° is linear along [110] direction as shown in Fig. 11.7b. The $(\sqrt{13} \times \sqrt{13})$ R33.7° has a five member "S" shaped units depicted in Fig. 11.7c, while DFT calculations (as yet not fully verified by experiment) suggest 8-member rings form a (3×3) structure shown in Fig. 11.7d. Finally, a second variant of the 4-member rings that comprise the $c(4 \times 2)$ is also the dominant structural feature for the $(\sqrt{5} \times \sqrt{5})$ R26.6° configuration, as shown in Fig. 11.7d. It should also be mentioned that while the (001) surface is dominated by octahedral Ti, the (110) contains very different tetrahedral units [54] and the (111) surface is even more complicated.

11.3.3 Nanostructured $SrTiO_3$

In addition to the periodic surface reconstructions discussed above, Ti-rich linear nanostructures have been obtained on the $SrTiO_3(001)$ surface by annealing $c(4 \times 2)$-reconstructed specimens in UHV [7, 42]. The linear nanostructures, termed 'nanolines'

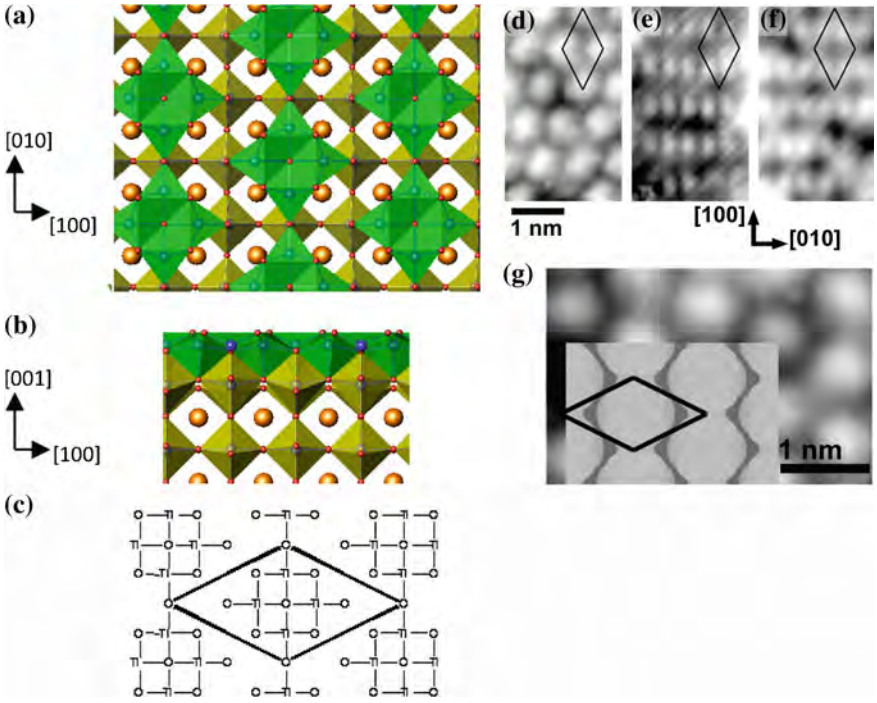

Fig. 11.6 Polyhedral representation of the $c(4 \times 2)$ structure is shown in **a** and **b** in which the TiO_5 polyhedra are shown in *green* and TiO_6 octahedra are olive (Sr = *gold*, Ti = *red*, O = *blue*). The *green* TiO_5 polyhedra decorate the surface, while TiO_6 octahedra exist below the surface layer. Image adapted from N. Erdman et al. showing plan view schematics of the overlayer **c** $c(4 \times 2)$ reconstruction. Reprinted (adapted) with permission from Erdman et al. [45]. Copyright (2003) American Chemical Society [45]. STM images of the $c(4 \times 2)$ in **d** ($V_s = 2.0$ V, $I_t = 0.1$ nA) and **e** ($V_s = 0.25$ V, $I_t = 1.0$ nA) respectively show the bias dependence of the reconstruction. The STM image in **f** shows a convolution of the two different electronic structures ($V_s = 0.45$ V, $I_t = 0.44$ nA). The STM images in **d**–**f** were adapted from Castell [42]. Reprinted from Castell [42]. Copyright (2002), with permission from Elsevier. **g** An experimental STM image ($V_s = 2.0$ V, $I_t = 0.1$ nA) with an overlaid STM simulation ($V_s = 2.0$ V). The STM simulation is derived from the structure depicted in **a**. Reprinted with permission from Becerra-Toledo et al. [53]. Copyright (2012), AIP Publishing LLC [53] (Color figure online)

are oriented along one of the <100> directions and have been observed via scanning tunnelling microscopy (STM). There are three types of nanolines: dilines (two rows) [42, 55], trilines (three rows), and tetralines (twice the width of a diline) [7], which exhibit (6×2), (8×2) and (12×2) periodicity respectively when found in close-packed domains. Notably, the polyhedral quartet motif is also an important part of all three nanoline surfaces [53].

Dilines, shown in Fig. 11.8a and b, are observed in isolation and in close-packed form, and coexist with $c(4 \times 2)$ terraces, which sit 2 Å lower than the dilines, corresponding to one atomic layer [42]. Auger electron spectra (AES) demonstrate that nanoline-covered $SrTiO_3(001)$ surfaces contain more Ti content than even

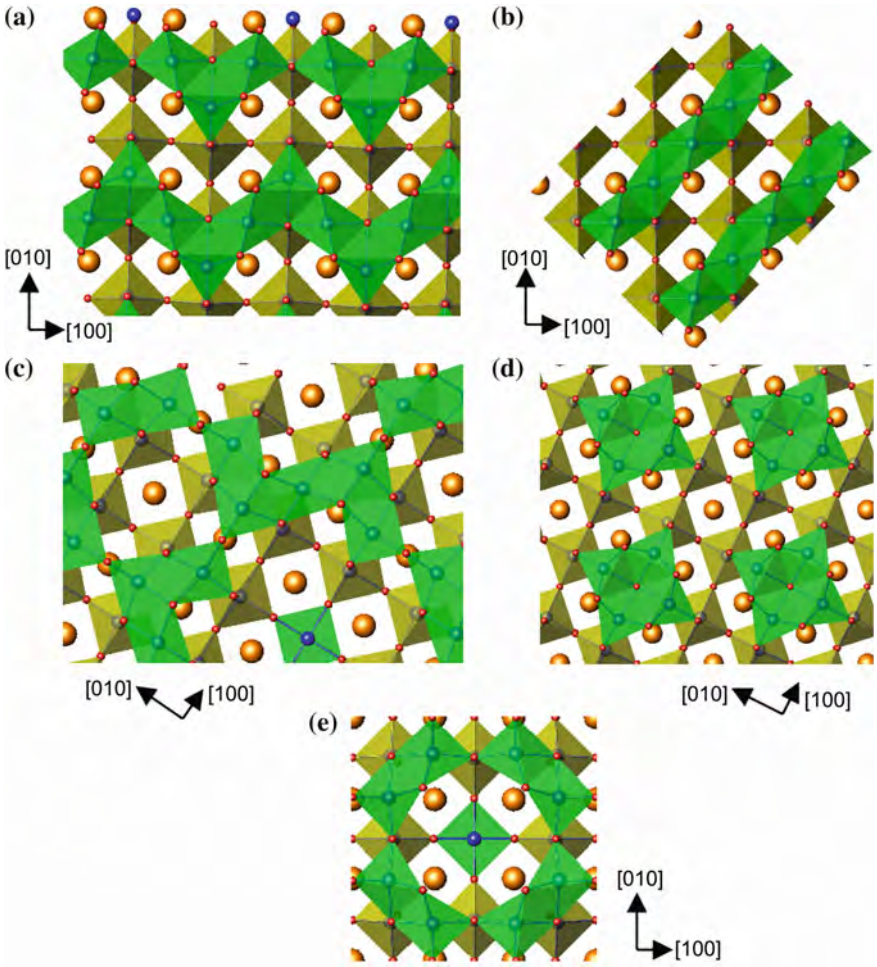

Fig. 11.7 Plan-view polyhedral representations of the **a** (2 × 2) reconstruction [46] and **b** ($\sqrt{2} \times \sqrt{2}$) R45° where TiO_5 polyhedra are *green* and TiO_6 octahedra are olive [46]. Reprinted from Warschkow et al. [46]. Copyright (2004), with permission from Elsevier. **c** ($\sqrt{13} \times \sqrt{13}$) R33.7° [48], **d** the ($\sqrt{5} \times \sqrt{5}$) R26.6° [48], **e** the (3 × 3) [48] (Ti = *blue*, O = *red*, Sr = *gold*). The *green* TiO_5 polyhedra decorate the TiO_x-terminated surface while the olive TiO_6 octahedra form the bulk structure. Reprinted figures with permission from Kienzle et al. [48]. Copyright (2011) by the American Physical Society (Color figure online)

double-layer TiO_2 rich reconstructions. Moreover, AES spectra are indicative of a predominant 4+ valence state for the surface Ti in nanoline surfaces [7]. These findings strongly suggest that the nanoline structures are terminated by three TiO_{2-x} layers. When in close-packed domains, dilines exhibit (6 × 2) periodicity and a ridge-and-valley configuration. Following this description, each diline consists of two parallel rows of bright round motifs, observed with STM under large positive

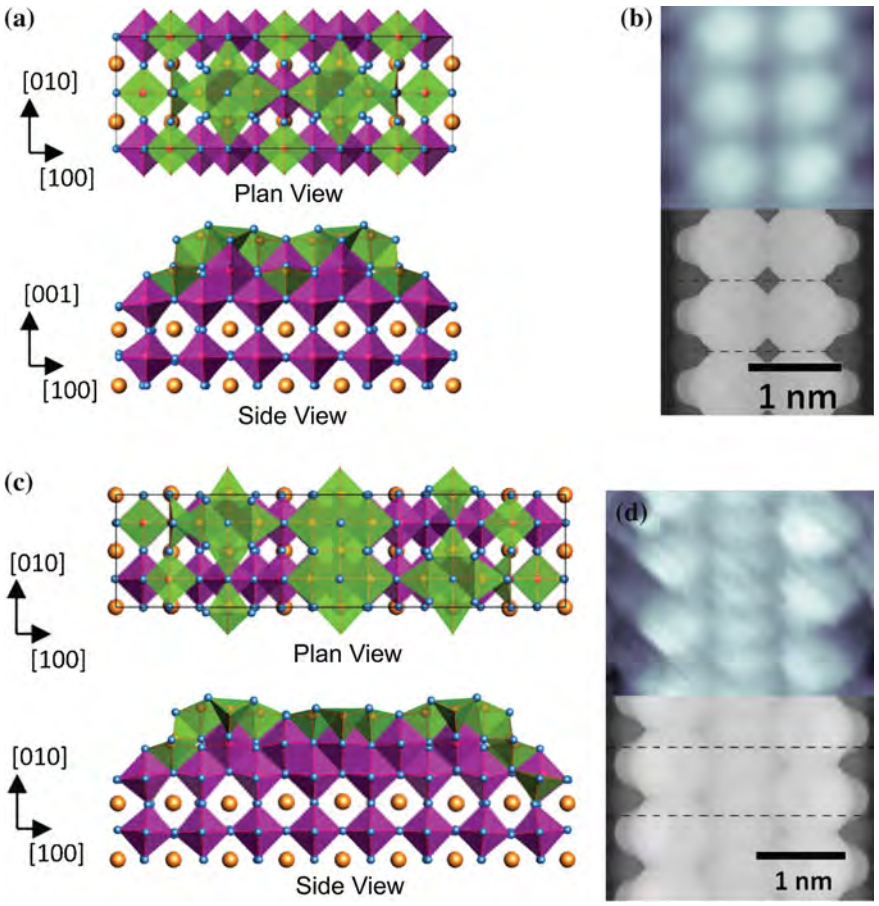

Fig. 11.8 **a** Polyhedral representation of the structure of a diline in the square configuration where TiO_6 octahedra are *purple* and TiO_5 polyhedra are *green* and a double-layer of TiO_6 octahedra exists below the surface layer. **b** An experimental STM image of a diline (V_s = 1.7 V, I_t = 0.05 nA) with the STM simulation of the structure depicted in **a** (V_s = 1.5 V) overlaid on the bottom. **c** Polyhedral representation of the structure of a triline nanostructure. **d** An STM image of the triline nanostructure (V_s = 2.23 V, I_t = 0.24 nA) with the STM simulation of the structure depicted in **c** overlaid on the bottom (V_s = 1.5 V). Reprinted with permission from Becerra-Toledo et al. [53]. Copyright (2012), AIP Publishing LLC [53] (Color figure online)

bias in Fig. 11.8b. Dilines adopt two configurations: (a) square, where the bright motifs from adjacent rows are aligned, and (b) zigzag, where the motifs in a row are shifted by one bulk unit cell along the length of the diline with respect to the neighbouring row. The distance between rows within a diline is 7.8 Å, which corresponds to exactly two bulk $SrTiO_3$ unit cells.

The bright, round motifs that comprise the dilines are the same size and shape as the STM features that characterize the $c(4 \times 2)$ surface. This is the polyhedral quartet motif of four edge-sharing TiO_5 polyhedra, registered to a bulk-like TiO_2

layer underneath. The $c(4 \times 2)$ atomic structure, determined via diffraction-based methods, has been verified through STM image simulations based on density functional theory (DFT) computations [53]. These simulations rely on a modification to the classical Tersoff-Hamann approximation [56] to extend it to large sample-tip bias. Moreover, the simulated images mirror the constant-current nature of experimental micrographs and account for the blurring effects of tip size and thermal vibrations. Tests also validated the chosen DFT parameters and the decision to exclude any bias-induced external electric field from the modelling [53].

The same methods have been employed to determine the atomic structure of the $SrTiO_3(100)$ dilines, by testing multiple structural candidates [53, 57]. Taking into account the observation that the $c(4 \times 2)$ is a precursor of (and coexists with) the dilines, and the similarity between their main STM features, the polyhedral quartet motif was incorporated into diline structural models, shown in Fig. 11.8a [53]. STM and AES data do force an important difference that the diline must consist of three, not two, TiO_{2-x} atomic layers at the surface. The $c(4 \times 2)$-like motifs specify the outermost atomic structure, corresponding to the "ridge" features, and they also constrain the atomic arrangement immediately beneath them. Due to energetic considerations, the ridge portion of the second layer must be much like a bulk-like TiO_2 layer, similar to the second layer of the $c(4 \times 2)$ surface reconstruction [53].

The "valley" portion of the diline, however, is significantly different from a bulk-like conformation, because the experimentally-measured corrugation in constant-current STM images requires access of the tip to a third layer [7]. The third layer is more difficult to probe, but it is expected to qualitatively adopt the same architecture as a bulk-like TiO_2 layer of $SrTiO_3(100)$. STM image simulations are shown in Fig. 11.8b compared to an experimental micrograph, from which it was determined that the second layer in the diline valley differed from a bulk-like TiO_2 arrangement in the following way: the Ti–O chain of atoms along the centre of the valley is removed, as are the second-layer O atoms which would have been bonded to the removed Ti atoms and aligned to the near-most quartet motif. For clarity, see Fig. 11.8a for a polyhedral representation of a diline under the "square" configuration.

Trilines are nanostructures that appear to be very similar to dilines, with the notable difference that their STM images incorporate a bright "backbone" between diline-like rows of bright round spots [7], shown in the top-half of Fig. 11.8d. The backbone consists of building blocks repeating periodically at single bulk unit cell intervals (3.9 Å) along the longitudinal direction [57]. Each backbone feature looks oval-like and has mirror symmetry along the transverse direction. The transverse distance between the backbone and either "diline-like" row corresponds to two bulk unit cells. When found in close-packed domains, trilines typically exhibit (8×2) periodicity. X-ray photoelectron spectroscopy (XPS) data shows the appearance of Ti^{2+} $2p$ peaks, which are not observed for diline-only surfaces [57]. Since the appearance of Ti^{2+} is the only difference between the dilines and trilines, this indicates that there is some reduced Ti in this portion of the triline architecture.

DFT-based STM image simulations, shown in the bottom-half of Fig. 11.8d, along with constraints from experimental data have been exploited to determine the atomic-scale triline structure, with special emphasis on the distinctive backbone.

The polyhedral representation of the solved triline structure under the "zigzag" configuration is shown in Fig. 11.8c. As can be seen, the backbone consists of checkerboard-like Ti–O arrangement [53], resulting again in edge-sharing TiO_5 polyhedra; this recurring pattern clearly constitutes a stabilization mechanism in this perovskite system. The top-layer within the backbone portion has a Ti_3O_5 composition, which is indicative of local Ti reduction; this is consistent with the XPS results [58]. Bond valence sum analysis, whose applicability has been shown to extend to surfaces [59], further confirm the presence of Ti backbone sites showing reduction comparable to standard Ti^{2+} materials [53]. The difference in stoichiometry between dilines and trilines allows for the accommodation of compositional variation on nanoline-decorated $SrTiO_3(100)$ surfaces.

11.4 Surface Defects

11.4.1 Defects at the Surface of $SrTiO_3$

Section 11.2 introduced bulk defects in $SrTiO_3$ including point defects and vacancy clusters. The surface structure of $SrTiO_3$ was briefly introduced in Sect. 11.3. We can now begin to understand how defects in $SrTiO_3$ appear at the surface and how these surface and near-surface defects influence the properties of the material. The most commonly attributed defect at the surface is an oxygen vacancy. It is easy to introduce oxygen vacancies into the perovskite oxides by vacuum annealing, ion bombardment and during growth. This line of research has been pursued for decades, and in early work on $SrTiO_3$ there was already an awareness of the role of oxygen vacancies [60]. The oxygen vacancy acts as an electron donor, and the presence of oxygen vacancies is typically inferred from the spectroscopic signature of Ti^{3+}. Recent work on vacuum-cleaved $SrTiO_3$ single crystals indicates that oxygen vacancies at the surface lead to the formation of a 2D electron gas, which has been observed with angle resolved photoemission spectroscopy (ARPES) [3, 61, 62]. More generally, by controlling the concentration of oxygen vacancies, the surface region can be switched from semiconducting to metallic [63].

11.4.2 Surface Vacancy Clusters

Informed by recent advancements in determining the structure of the $SrTiO_3$ surface, we can look with renewed insight at the structure of defects in the surface region. In particular, the presence of large defect clusters seems to be an important defect-formation mechanism, both in the bulk [10, 20] and on the surface [53, 57]. Here, we will focus on two defects—the absence of a polyhedral quartet structural motif across several different surfaces, and a defect in the central row of the triline.

11.4.3 Polyhedral Quartet Defects

An STM simulation of two diline nanostructures is shown in Fig. 11.9a, with a ball and stick representation of the top-most layer shown over-laid in the corner. In Fig. 11.9b, an STM image of an isolated diline is shown. The black arrow in

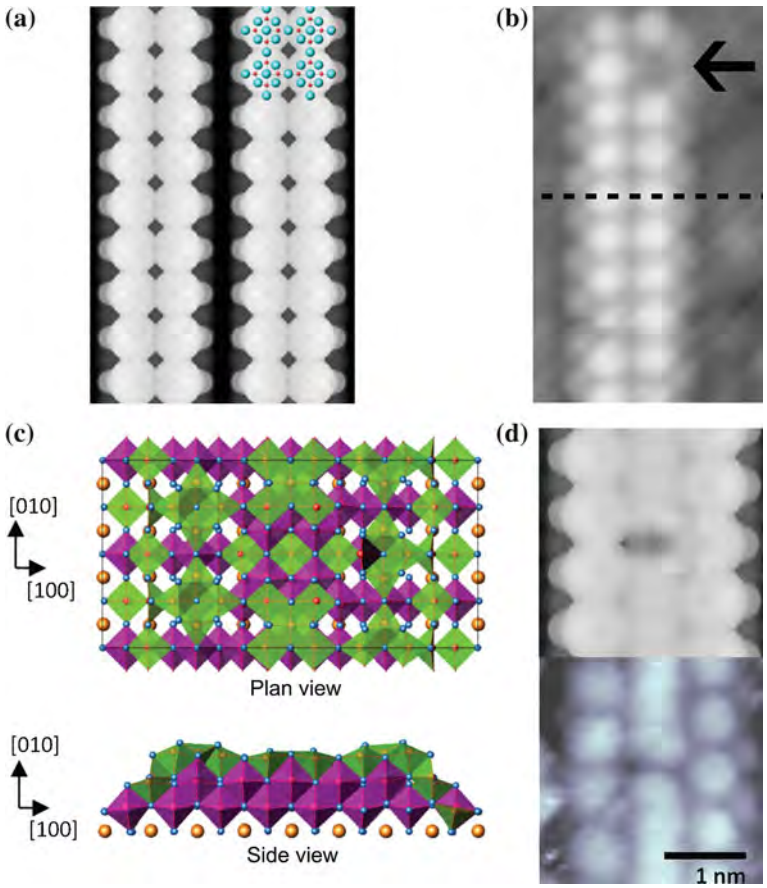

Fig. 11.9 **a** STM simulations of a diline nanostructured surface, with a ball and stick structure of the top-most layer overlaid in the top-right corner (Ti = *red*, O = *blue*) [58]. **b** An STM image showing an isolated diline on a $c(4 \times 2)$ surface [42]. The *arrow* indicates the presence of a defect at the site of a polyhedral quartet motif. Reprinted from Castell [42]. Copyright (2002), with permission from Elsevier. **c** The structure of a triline defect in the central row, as determined by first principles calculations, adapted from [53] where TiO_6 octahedra are *purple* and TiO_5 polyhedra are *green* (Sr = *gold*, oxygen = *blue*, Ti = *red*). A double-layer of TiO_6 octahedra exists below the surface layer. Reprinted with permission from Becerra-Toledo et al. [53]. Copyright (2012), AIP Publishing LLC **d** An STM simulation of the triline defect in (**c**) is compared to an STM image of a defect in the central row of the triline [57]. Reprinted figure with permission from Marshall et al. [57]. Copyright (2011) by the American Physical Society

Fig. 11.9b denotes the absence of the polyhedral quartet structural unit along the side row of the diline. This type of defect is often observed on surfaces decorated by nanolines. While the details of the defect in Fig. 11.9b have not been fully studied, the images suggests that this corresponds to the absence of a polyhedral quartet unit. This defect is similar in appearance to defects present on the $c(4 \times 2)$ reconstruction, as well as those found in the side-rows of the trilines and tetralines.

11.4.4 Triline Defects

The triline nanostructure exhibits two types of defect clusters, a defect cluster in the side-row, and a defect cluster in the central row. The first, which is nearly identical to the diline, is the absence of a side-row spot that corresponds to a polyhedral quartet unit. While the precise details of this defect are unknown, its prevalence on four different surfaces $c(4 \times 2)$, dilines, trilines and tetralines, is indicative that the fundamental nature of the polyhedral quartet motif extends to its absence, in the form of a defect cluster. If the dark spot in the STM images is caused by a missing top-layer, then the defect cluster would consist of Ti_4O_8.

Experimental STM images have revealed a distinctive backbone defect in triline structures [57]. In constant-current micrographs, the defect shows up as a missing backbone repeat unit. That is, a single bright oval-like feature is replaced by a dark feature (or depression) with the width corresponding to a single bulk unit cell [53, 57]. Figure 11.9c shows the plan-view polyhedral atomistic structure of a Ti_4O_3 defect cluster in the central row of the triline as well as a side view of this same structure [53]. Each defect has local mirror symmetry along both the longitudinal and transverse triline directions. STM simulations can be compared with experimental STM images in Fig. 11.9d, and reveal an excellent match between the experimental and simulated structures. Diffusion of the cluster defect to a side-row is not observed, but diffusion does occur along the length of the triline. The confined nature of cluster diffusion lends itself to study with high-temperature STM.

Symmetry constraints and a large measured diffusion activation energy rule out the possibility of the defect consisting of a single atom (Ti or O). The arrangement that best matches the experimental STM micrographs, while satisfying all other conditions, is shown in Fig. 11.9c and d under the "zigzag" triline configuration. In this structure, a quartet of top-layer Ti atoms is removed, along with three collinear top-layer O along the middle of the defect, originally bonded to the absent Ti. However, the four removed Ti are not truly eliminated, but merely relocated: each of the Ti atoms is displaced to the layer beneath, occupying octahedral sites that are otherwise vacant [53]. In this manner top-layer O atoms along the defect perimeter are coordinated to two Ti atoms, instead of just one, which would lead to high structural instability and features in the STM image simulations that are not observed experimentally.

The structure of the defect was inferred from STM images, using the symmetry constraints and large diffusion energy as a guide, as well as the measured valence

state of Ti in the system [57]. Several candidate structures were simulated using DFT, and the results compared to experimental STM micrographs. A poor match between important features of the STM images ruled out several structures [53]. The common side-lobe features are similar to the $c(4 \times 2)$ surface which led to the notion of the polyhedral quartet motif structure for the side lobes. The presence of Ti^{2+} in XPS measurements enforced a requirement of Ti^{2+} in the background. With this established, the only candidate defect structures that replicated the features observed in the STM images were defect clusters. A Ti_4O_3 defect cluster produced the best agreement between theory and experiment, and fits within an emerging understanding of the role of clusters in the $SrTiO_3$ surface region [10].

11.5 Defect Diffusion

11.5.1 Point Defect Diffusion

While scant attention has been devoted to measuring the kinetics of defects at the surface of $SrTiO_3$, there have been several studies on the diffusion of bulk defects, presenting a wide range of values in the literature. For instance, the high temperature diffusion of Ti in donor-doped (La) $SrTiO_3$ was found to be 3.3 eV per Ti atom [64]. In contrast, a simulation of titanium vacancy diffusion yielded an activation energy, E_a = 11.6 eV for Ti^{4+} vacancies and E_a = 2.5 eV for Sr^{2+} vacancies [14]. These values are significantly higher than older studies that found activation energies of Ea = 4.9 eV for Ti^{4+} and Sr^{2+} vacancy diffusion [65]. More recent work on Nb-doped $SrTiO_3$ posited values of 1.2 eV for Sr^{2+} and Ti^{4+} vacancies [66]. Additionally, work on a related material system, Nb-doped $BaTiO_3$, confirmed work by Lewis and Catlow that Ti^{4+} vacancies are more energetically favourable than Ba^{2+} cation vacancies because of strain considerations [67, 68]. Separate experimental studies have found that the activation energy for the diffusion of oxygen in $SrTiO_3$ is less than 1 eV [69, 70]. While measurements of the activation energy of point defect diffusion are useful for comparative purposes, the wide range of values in the literature limits their utility.

11.5.2 Diffusion of Defect Clusters

In Sect. 11.4 we introduced some of the defects and vacancy clusters that form on the nanostructured surface of $SrTiO_3$. One such defect forms in the central row of the triline nanostructure and appears as a dark spot. DFT calculations revealed that the dark spot corresponds to a Ti_4O_3 defect cluster. Because the central row, or backbone, of the triline is a line, it is therefore appropriate to model the diffusion of the Ti_4O_3 defect cluster using a 1D diffusion model. Modelling defect diffusion can

be complicated, but the 1D approximation simplifies matters considerably. Such a model relies on determining the probability of the diffusing species being located at a position x, and is given by [71–73]:

$$P_x(ht) = \exp(-2ht) I_x(2ht) \tag{11.2}$$

where P_x is the probability, h is the hopping rate, t is the time between measurements, and I_x are modified Bessel functions of the first kind. The mean square displacement, $\langle \delta x^2 \rangle$, of the probability distribution is given by [72]:

$$\langle \delta x^2 \rangle = 2ht \tag{11.3}$$

From this, by determining the displacement of a defect as a function of time, t, it is readily possible to determine the hopping rate. To accomplish this in the studies of surface defects using an instrument such as the STM, the defect is observed in two isothermal STM images that are taken an arbitrary time, t, apart. In order to avoid the effects of thermal drift in the image, such an experiment necessitates a long stabilization period to allow the tip and sample to thermally equilibrate.

For defects that experience discrete displacements corresponding to an integer multiple of the underlying lattice, the general rate of diffusion can be expressed in terms of the hopping rate, h. Constructing a semilog plot of the hopping rate against the inverse of temperature facilitates fitting with the Arrhenius diffusion equation. The activation energy, E_a and the exponential prefactor v are obtained from the resultant fit. The Arrhenius diffusion equation is:

$$h = v \exp\left(-E_a / k_B T\right) \tag{11.4}$$

where h is the hopping rate, k_B is Boltzmann's constant, and T is the temperature.

The ability to measure defect diffusion in terms of a series of hops along an atomic lattice requires STMs with high thermal stabilities and 'fast' scanning times. Study of fast surface dynamics was only possible with the development of scanning tunnelling microscopes that had the ability to capture multiple frames per second, as first developed by the Aarhus group [74]. An early example is work by Linderoth et al. who studied diffusion of Pt atoms on the surface of reconstructed Pt(110) [75]. The technique of using isothermal rapid-scanning STM has since been applied to a variety of materials systems in order to observe 1D diffusion of defects and atoms [72], including on the nanostructured surface of $SrTiO_3(100)$ [57].

STM images taken at 518 °C of two triline nanostructures separated by a diline are shown in Fig. 11.10a–d. The backbone of the triline is visible in these images as a bright line comprised of spots that are one unit cell apart. The black arrows in Fig. 11.10a each indicate the absence of one of the bright spots, which is ascribed to be a Ti_4O_3 defect cluster in Sect. 11.4. Isothermal STM images of the same location taken 90 s apart are shown in Fig. 11.10b–d, where the black arrows denote the starting position of the vacancy cluster in Fig. 11.10a. These images show the position of the vacancy cluster moving along the length of the triline backbone. The vacancy clusters

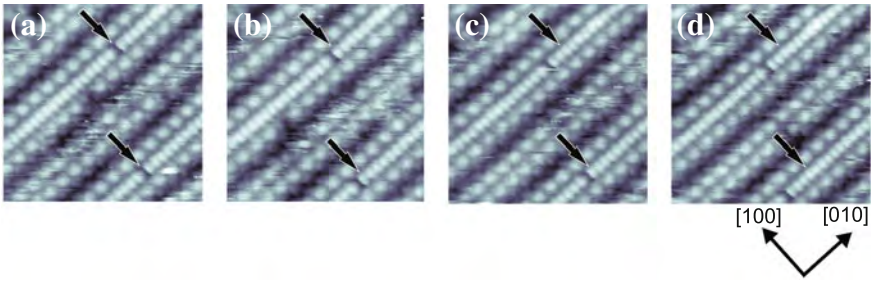

Fig. 11.10 Four isothermal STM images take at 90 s intervals of a triline nanostructured surface at a constant temperature of 518 °C. **a** The *arrows* indicate defects in the central row of the triline. **b–d** The *arrows* denote the starting position of the defects (9.5 × 9.5 nm^2, V_s = +1.87 V, I_t = 0.24 nA). Reprinted figure with permission from Marshall et al. [57]. Copyright (2011) by the American Physical Society [21]

are not observed to diffuse from the triline backbone to either of the side rows, reinforcing the validity of the 1D-model for this system. In these images measuring the displacement of the vacancy cluster is a matter of counting the number of spots.

A plot of the vacancy cluster hopping rate versus the inverse temperature is shown in Fig. 11.11, while the temperature in degrees Celsius is shown on the top *x*-axis. For each point, the hopping rate is determined by measuring the displacement of 50–75 hopping events, while excluding hopping events that could potentially interact with nearby vacancy clusters on the same triline, or with the triline end-points. The horizontal error bars are due to an estimated uncertainty in the temperature measurements, while the vertical error bars arise from measurements of

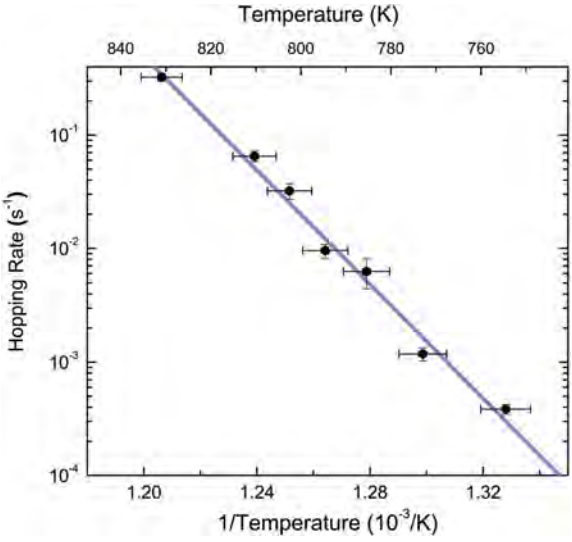

Fig. 11.11 A semilog Arrhenius diffusion plot of the hopping rate versus reciprocal temperature (1/T). Fitting to this plot facilitates extraction of the defect diffusion energy. Reprinted figure with permission from Marshall et al. [57]. Copyright (2011) by the American Physical Society [57]

the cluster displacement. Observing a sufficiently large number of hopping events at a series of different temperatures allows the measured hopping rate to be fitted with the Arrhenius diffusion equation described in 11.4. This resulted in an activation energy of $E_a = 4.98 \pm 0.17$ eV [57].

Careful analysis of the atomic structure of the triline facilitates speculation of the mechanism of cluster diffusion. Figure 11.12 shows a schematic of the ball-and-stick representation of only the central backbone of the triline. In practice, the triline backbone defect consists of three effective O vacancies, in addition to the relocation of four top-layer Ti atoms to subsurface sites. The symmetry constraints and the electronic structure, as probed by STM, dictate the need for a complicated defect. This is further re-enforced by the large diffusion activation barrier, which is much larger than for single-atom surface diffusion. As reference, the activation energy for the bulk diffusion of an oxygen vacancy in $SrTiO_3$ is 0.4–0.6 eV [76, 77], and surface diffusion is indeed easier: the analogous value on a TiO_2-truncated $SrTiO_3$(001) surface is estimated to be 0.1 eV [77].

This structure does require a complicated 3D mechanism for the (effectively 1D) translation of the defect along the length of the triline backbone [57]. The collaborative nature of such a mechanism is illustrated in Fig. 11.12 for a displacement across one bulk unit cell. As seen in the schematic, defect motion requires three second-layer Ti atoms to move to top-layer sites, while three top-layer Ti atoms concurrently jump to octahedral sites in the second atomic layer. Furthermore, three oxygen atoms must simultaneously hop across the topmost layer to new sites. This convoluted diffusion involving the synchronized transport of nine atoms is consistent with the large value of the measured 1D diffusion activation energy for the triline backbone defect [57].

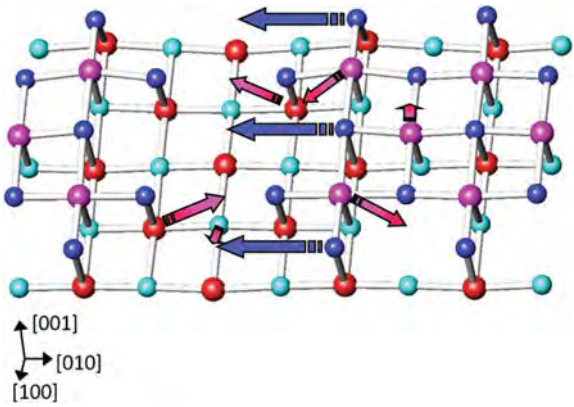

Fig. 11.12 A schematic *ball* and *stick* representation of the top two layers of a 2 × 4 triline supercell showing Ti_4O_3 defect cluster diffusion. Surface Ti are shown in *pink*, subsurface Ti are in *red*, surface O are in *blue* while subsurface O atoms are *light blue*. The *arrows* indicate where atoms move during the course of defect diffusion. Reprinted with permission from Becerra-Toledo et al. [53]. Copyright (2012), AIP Publishing LLC [53] (Color figure online)

11.6 Conclusions

$SrTiO_3$ is commonly used as a substrate for thin film growth and is a model system for the study of defects in the perovskite oxides. Over the last decade, tremendous progress has been made in solving the structure of the various reconstructed and nanostructured surfaces of $SrTiO_3$(001). This has facilitated the study of the atomic structure of defects at the surface and in the bulk. Comprehensive knowledge of the atomic and electronic structure of these defects, as well as how defects diffuse, is of critical importance for technological applications of this material. For instance, defects in $SrTiO_3$ induce ferroelectricity, blue light emission and localised conduction. Defects are also relevant to the development of insulating high-k dielectrics, and resistive memory devices. Finally, defects in nanostructured surface phases may be of importance for catalysis. Studies of defects in $SrTiO_3$ are generally applicable to similar materials systems and offer a useful starting point when studying other perovskite oxides.

References

1. D. Kan, T. Terashima, R. Kanda, A. Masuno, K. Tanaka, S. Chu, H. Kan, A. Ishizumi, Y. Kanemitsu, Y. Shimakawa, M. Takano, Blue-light emission at room temperature from Ar^+-irradiated $SrTiO_3$. Nat. Mater. **4**, 816–819 (2005)
2. K. Szot, W. Speier, G. Bihlmayer, R. Waser, Switching the electrical resistance of individual dislocations in single-crystalline $SrTiO_3$. Nat. Mater. **5**, 312–320 (2006)
3. A.F. Santander-Syro, O. Copie, T. Kondo, F. Fortuna, S. Pailhès, R. Weht, X.G. Qiu, F. Bertran, A. Nicolaou, A. Taleb-Ibrahimi, P. Le Fèvre, G. Herranz, M. Bibes, N. Reyren, Y. Apertet, P. Lecoeur, A. Barthélémy, M.J. Rozenberg, Two-dimensional electron gas with universal subbands at the surface of $SrTiO_3$. Nature **469**, 189–193 (2011)
4. J. Robertson, High dielectric constant gate oxides for metal oxide Si transistors. Rep. Prog. Phys. **69**, 327 (2006)
5. M. Janousch, G.I. Meijer, U. Staub, B. Delley, S.F. Karg, B.P. Andreasson, Role of oxygen vacancies in Cr-doped $SrTiO_3$ for resistance-change memory. Adv. Mater. **19**, 2232–2235 (2007)
6. E. Ertekin, V. Srinivasan, J. Ravichandran, P.B. Rossen, W. Siemons, A. Majumdar, R. Ramesh, J.C. Grossman, Interplay between intrinsic defects, doping, and free carrier concentration in $SrTiO_3$ thin films. Phys. Rev. B **85**, 195460 (2012)
7. D.S. Deak, F. Silly, D.T. Newell, M.R. Castell, Ordering of TiO_2-based nanostructures on $SrTiO_3$(001) surfaces. J. Phys. Chem. B **110**, 9246–9251 (2006)
8. O.N. Tufte, P.W. Chapman, Electron mobility in semiconducting strontium titanate. Phys. Rev. B **155**, 796–802 (1967)
9. M. Choi, F. Oba, Y. Kumagai, I. Tanaka, Anti-ferrodistortive-like oxygen-octahedron rotation induced by the oxygen vacancy in cubic $SrTiO_3$. Adv. Mater. **25**, 86–90 (2013)
10. D.J. Keeble, S. Wicklein, R. Dittmann, L. Ravelli, R.A. Mackie, W. Egger, Identification of A-and B-site cation vacancy defects in perovskite oxide thin films. Phys. Rev. Lett. **105**, 226102 (2010)
11. M. Choi, F. Oba, I. Tanaka, Role of Ti antisitelike defects in $SrTiO_3$. Phys. Rev. Lett. **103**, 185502 (2009)

12. Y.Y. Guo, H.M. Liu, D.P. Yu, J.-M. Liu, Ferroelectricity and superparamagnetism in Sr/Ti nonstoichiometric $SrTiO_3$. Phys Rev B **85**, 104108 (2012)
13. H.W. Jang, A. Kumar, S. Denev, M.D. Biegalski, P. Maksymovych, C.W. Bark, C.T. Nelson, C.M. Folkman, S.H. Baek, N. Balke, C.M. Brooks, D.A. Tenne, D.G. Schlom, L.Q. Chen, X.Q. Pan, S.V. Kalinin, V. Gopalan, C.B. Eom, Ferroelectricity in strain-free $SrTiO_3$ thin films. Phys. Rev. Lett. **104**, 197601 (2010)
14. M.J. Akhtar, Z.U.N. Akhtar, R.A. Jackson, C.R.A. Catlow, Computer simulation studies of strontium titanate. J. Am. Ceram. Soc. **78**, 421–428 (1995)
15. H.L. Tuller, S.R. Bishop, Point defects in oxides: tailoring materials through defect engineering. Ann. Rev. Mater. Res. **41**, 369–398 (2011)
16. D.A. Muller, N. Nakagawa, A. Ohtomo, J.L. Grazul, H.Y. Hwang, Atomic-scale imaging of nanoengineered oxygen vacancy profiles in $SrTiO_3$. Nature **430**, 657–661 (2004)
17. D.D. Cuong, B. Lee, K.M. Choi, H.-S. Ahn, S. Han, J. Lee, Oxygen vacancy clustering and electron localization in oxygen-deficient $SrTiO_3$: LDA+U study. Phys. Rev. Lett. **98**, 115503 (2007)
18. Y. Tokuda, S. Kobayashi, T. Ohnishi, T. Mizoguchi, N. Shibata, Y. Ikuhara, T. Yamamoto, Strontium vacancy clustering in Ti-excess $SrTiO_3$ thin film. Appl. Phys. Lett. **99**, 033110 (2011)
19. Y.S. Kim, J. Kim, S.J. Moon, W.S. Choi, Y.J. Chang, J.-G. Yoon, J. Yu, J.-S. Chung, T.W. Noh, Localized electronic states induced by defects and possible origin of ferroelectricity in strontium titanate thin films. Appl. Phys. Lett. **94**, 202906 (2009)
20. D.J. Keeble, R.A. Mackie, W. Egger, B. Löwe, P. Pikart, C. Hugenschmidt, T.J. Jackson, Identification of vacancy defects in a thin film perovskite oxide. Phys. Rev. B **81**, 064102 (2010)
21. M.S.J. Marshall, M.R. Castell, Shape transitions of epitaxial islands during strained layer growth: anatase $TiO_2(001)$ on $SrTiO_3(001)$. Phys. Rev. Lett. **102**, 146102 (2009)
22. F. Silly, M.R. Castell, Formation of single-domain anatase $TiO_2(001)$-(1×4) islands on $SrTiO_3(001)$ after thermal annealing. Appl. Phys. Lett. **85**, 3223–3225 (2004)
23. K. Szot, W. Speier, Surfaces of reduced and oxidized $SrTiO_3$ from atomic force microscopy. Phys. Rev. B **60**, 5909–5926 (1999)
24. Y. Liang, D.A. Bonnell, Atomic structures of reduced $SrTiO_3(001)$ surfaces. Surf. Sci. Lett. **285**, L510–516 (1993)
25. Y. Liang, D.A. Bonnell, Effects of variations in stoichiometry on the surface structure of $SrTiO_3(001)$. J. Am. Ceram. Soc. **78**, 2633–2640 (1995)
26. R. Meyer, R. Waser, J. Helmbold, G. Borchardt, Cationic surface segregation in donor-doped $SrTiO_3$ under oxidizing conditions. J. Electroceram. **9**, 101–110 (2002)
27. S.N. Ruddlesden, P. Popper, New compounds of the K_2NiF_4 type. Acta Cryst. **10**, 538–539 (1957)
28. S.N. Ruddlesden, P. Popper, The compound $Sr_3Ti_2O_7$ and its structure. Acta Cryst. **11**, 54–55 (1958)
29. K. Szot, M. Pawelczyk, J. Herion, C. Freiburg, J. Albers, R. Waser, J. Hulliger, J. Kwapulinski, J. Dec, Nature of the surface layer in ABO_3-type perovskites at elevated temperatures. Appl. Phys. A **62**, 335–343 (1996)
30. K.H. Lee, S.W. Kim, H. Ohta, K. Koumoto, Ruddlesden-Popper phases as thermoelectric oxides: Nb-doped SrO $(SrTiO_3)_n$ (n = 1, 2). J. Appl. Phys. **100**, 063717 (2006)
31. N.D. Orloff, W. Tian, C.J. Fennie, C.H. Lee, D. Gu, J. Mateu, X.X. Xi, K.M. Rabe, D.G. Schlom, I. Takeuchi, J.C. Booth, Broadband dielectric spectroscopy of Ruddlesden-Popper $Sr_{n+1}Ti_nO_{3n+1}$ (n = 1, 2, 3) thin films. Appl. Phys. Lett. **94**, 042908 (2009)
32. J.H. Haeni, C.D. Theis, D.G. Schlom, W. Tian, X.Q. Pan, H. Chang, I. Takeuchi, X.-D. Xiang, Epitaxial growth of the first five members of the $Sr_{n+1}Ti_nO_{3n+1}$ Ruddlesden-Popper homologous series. Appl. Phys. Lett. **78**, 3292–3294 (2001)
33. C. Noguera, Theoretical investigation of the Ruddlesden-Popper compounds $Sr_{n+1}Ti_nO_{3n+1}$ (n = 1−3). Phil. Mag. Lett. **80**, 173–180 (2000)

34. T. Birol, N.A. Benedek, C.J. Fennie, Interface control of emergent ferroic order in Ruddlesden-Popper $Sr_{n+1}Ti_nO_{3n+1}$. Phys. Rev. Lett. **107**, 257602 (2011)
35. K. Szot, W. Speier, R. Carius, U. Zastrow, W. Beyer, Localized metallic conductivity and self-healing during thermal reduction of $SrTiO_3$. Phys. Rev. Lett. **88**, 075508 (2002)
36. S. Menzel, M. Waters, A. Marchewka, U. Böttger, R. Dittmann, R. Waser, Origin of the ultra-nonlinear switching kinetics in oxide-based resistive switches. Adv. Funct. Mater. **21**, 4487–4492 (2011)
37. D.W. Reagor, V.Y. Butko, Highly conductive nanolayers on strontium titanate produced by preferential ion-beam etching. Nature Mater **4**, 593–596 (2005)
38. D. Kan, R. Kanda, Y. Kanemitsu, Y. Shimakawa, M. Takano, T. Terashima, A. Ishizumi, Blue luminescence from electron-doped $SrTiO_3$. Appl. Phys. Lett. **88**, 191916 (2006)
39. H. Yasuda, Y. Kanemitsu, Dynamics of nonlinear blue photoluminescence and auger recombination in $SrTiO_3$. Phys. Rev. B **77**, 193202 (2008)
40. J.M.E. Harper, J.J. Cuomo, H.R. Kaufman, Technology and applications of broad-beam ion sources used in sputtering. Part II. Applications. J. Vac. Sci. Tech **21**, 737–756 (1982)
41. M.R. Castell, Scanning tunneling microscopy of reconstructions on the $SrTiO_3(001)$ surface. Surf. Sci. **505**, 1–13 (2002)
42. M.R. Castell, Nanostructures on the $SrTiO_3(001)$ surface studied by STM. Surf. Sci. **516**, 33–42 (2002)
43. K. Johnston, M.R. Castell, A.T. Paxton, M.W. Finnis, $SrTiO_3(001)(2 \times 1)$ reconstructions: first-principles calculations of surface energy and atomic structure compared with scanning tunneling microscopy images. Phys. Rev. B **70**, 085415 (2004)
44. N. Erdman, K.R. Poeppelmeier, M. Asta, O. Warschkow, D.E. Ellis, L.D. Marks, The structure and chemistry of the TiO_2-rich surface of $SrTiO_3(001)$. Nature **419**, 55–58 (2002)
45. N. Erdman, O. Warschkow, M. Asta, K.R. Poeppelmeier, D.E. Ellis, L.D. Marks, Surface structures of $SrTiO_3(001)$: a TiO_2-rich reconstruction with a $c(4 \times 2)$ unit cell. J. Am. Chem. Soc. **125**, 10050–10056 (2003)
46. O. Warschkow, M. Asta, N. Erdman, K.R. Poeppelmeier, D.E. Ellis, L.D. Marks, TiO_2-rich reconstructions of $SrTiO_3(001)$: a theoretical study of structural patterns. Surf. Sci. **573**, 446–456 (2004)
47. D. Keeble, R. Mackie, W. Egger, B. Löwe, P. Pikart, C. Hugenschmidt, T. Jackson, Identification of vacancy defects in a thin film perovskite oxide. Phys. Rev. B **81**, 064102 (2010)
48. D.M. Kienzle, A.E. Becerra-Toledo, L.D. Marks, Vacant-site octahedral tilings on $SrTiO_3(001)$, the $(\sqrt{1}3 \times \sqrt{1}3)$ R33.7° surface, and related structures. Phys. Rev. Lett. **106**, 176102 (2011)
49. F. Li, Z. Wang, S. Meng, Y. Sun, J. Yang, Q. Guo, J. Guo, Reversible transition between thermodynamically stable phases with low density of oxygen vacancies on the $SrTiO_3(110)$ surface. Phys. Rev. Lett. **107**, 036103 (2011)
50. H. Tanaka, T. Matsumoto, T. Kawai, S. Kawai, Surface structure and electronic property of reduced $SrTiO_3(100)$ surface observed by scanning tunneling microscopy/spectroscopy. Jap. J. App. Phys. **32**, 1405 (1993)
51. T. Kubo, H. Nozoye, Surface structure of $SrTiO_3(100)$-$(\sqrt{5} \times \sqrt{5})$-R 26.6°. Phys. Rev. Lett. **86**, 1801 (2001)
52. G.-Z. Zhu, G. Radtke, G.A. Botton, Bonding and structure of a reconstructed (001) surface of $SrTiO_3$ from TEM. Nature **490**, 384–387 (2012)
53. A.E. Becerra-Toledo, M.S.J. Marshall, M.R. Castell, L.D. Marks, $c(4 \times 2)$ and related structural units on the $SrTiO_3(001)$ surface: scanning tunneling microscopy, density functional theory, and atomic structure. J. Chem. Phys. **136**, 214701–214709 (2012)
54. J.A. Enterkin, A.K. Subramanian, B.C. Russell, M.R. Castell, K.R. Poeppelmeier, L.D. Marks, A homologous series of structures on the surface of $SrTiO_3(110)$. Nat. Mater. **9**, 245–248 (2010)
55. H.L. Marsh, D.S. Deak, F. Silly, A.I. Kirkland, M.R. Castell, Hot STM of nanostructure dynamics on $SrTiO_3(001)$. Nanotechnology **17**, 3543–3548 (2006)

56. J. Tersoff, D.R. Hamann, Theory and application for the scanning tunneling microscope. Phys. Rev. Lett. **50**, 1998–2001 (1983)
57. M.S.J. Marshall, A.E. Becerra-Toledo, L.D. Marks, M.R. Castell, Surface and defect structure of oxide nanowires on $SrTiO_3$. Phys. Rev. Lett. **107**, 086102 (2011)
58. M.S.J. Marshall, A.E. Becerra-Toledo, D.J. Payne, R.G. Egdell, L.D. Marks, M.R. Castell, Structure and composition of linear TiO_x nanostructures on $SrTiO_3$(001). Phys. Rev. B **86**, 125416 (2012)
59. J.A. Enterkin, A.E. Becerra-Toledo, K.R. Poeppelmeier, L.D. Marks, A chemical approach to understanding oxide surfaces. Surf. Sci. **606**, 344–355 (2012)
60. V.E. Henrich, G. Dresselhaus, H.J. Zeiger, Surface defects and the electronic structure of $SrTiO_3$ surfaces. Phys. Rev. B **17**, 4908–4921 (1978)
61. W. Meevasana, P.D.C. King, R.H. He, S.-K. Mo, M. Hashimoto, A. Tamai, P. Songsiriritthigul, F. Baumberger, Z.-X. Shen, Creation and control of a two-dimensional electron liquid at the bare $SrTiO_3$ surface. Nat. Mater. **10**, 114–118 (2011)
62. J. Shen, H. Lee, R. Valentí, H.O. Jeschke, Ab initio study of the two-dimensional metallic state at the surface of $SrTiO_3$: importance of oxygen vacancies. Phys. Rev. B **86**, 195119 (2012)
63. K. Takeyasu, K. Fukada, M. Matsumoto, K. Fukutani, Control of the surface electronic structure of $SrTiO_3$(001) by modulation of the density of oxygen vacancies. J. Phys.: Condens. Matter **25**, 162202 (2013)
64. K. Gömann, G. Borchardt, A. Gunhold, W. Maus-Friedrichs, H. Baumann, Ti diffusion in La-doped $SrTiO_3$ single crystals. Phys. Chem. Chem. Phys. **6**, 3639–3644 (2004)
65. W.H. Rhodes, W.D. Kingery, Dislocation dependence of cationic diffusion in $SrTiO_3$. J. Am. Ceram. Soc. **49**, 521–526 (1966)
66. P. Pasierb, S. Komornicki, M. Rekas, Comparison of the chemical diffusion of undoped and Nb-doped $SrTiO_3$. J. Phys. Chem. Solids **60**, 1835–1844 (1999)
67. G.V. Lewis, C.R.A. Catlow, Potential models for ionic oxides. J. Phys. C: Solid State Phys. **18**, 1149–1161 (1985)
68. T.B. Wu, J.N. Lin, Transition of compensating defect mode in niobium-doped barium titanate. J. Am. Ceram. Soc. **77**, 759–764 (1994)
69. A.E. Paladino, Oxidation kinetics of single-crystal $SrTiO_3$. J. Am. Ceram. Soc. **48**, 476–478 (1965)
70. L.C. Walters, R.E. Grace, Formation of point defects in strontium titanate. J. Phys. Chem. Solids **28**, 239–244 (1967)
71. J.D. Wrigley, M.E. Twigg, G. Ehrlich, Lattice walks by long jumps. J. Chem. Phys. **93**, 2885 (1990)
72. Z. Zhang, Q. Ge, S.-C. Li, B.D. Kay, J.M. White, Z. Dohnálek, Imaging Intrinsic Diffusion of Bridge-Bonded Oxygen Vacancies on TiO_2(110). Phys. Rev. Lett. **99**, 126105 (2007)
73. M.S.J. Marshall, *Nanostructured Strontium Titanate Surfaces*. DPhil Thesis, University of Oxford, Oxford, UK (2009)
74. F. Besenbacher, E. Lægsgaard, I. Stensgaard, Fast-scanning STM studies. Mater. Today **8**, 26–30 (2005)
75. T.R. Linderoth, S. Horch, E. Lægsgaard, I. Stensgaard, F. Besenbacher, Surface diffusion of Pt on Pt(110): Arrhenius Behavior of Long Jumps. Phys. Rev. Lett. **78**, 4978 (1997)
76. M. Lontsi-Fomena, A. Villesuzanne, J.-P. Doumerc, C. Frayret, M. Pouchard, A density functional theory study of oxygen diffusion in $LaAlO_3$ and $SrTiO_3$. Comput. Mater. Sci. **44**, 53–60 (2008)
77. J. Carrasco, F. Illas, N. Lopez, E.A. Kotomin, Y.F. Zhukovskii, R.A. Evarestov, Y.A. Mastrikov, S. Piskunov, J. Maier, First-principles calculations of the atomic and electronic structure of F centers in the bulk and on the (001) surface of $SrTiO_3$. Phys. Rev. B **73**, 064106 (2006)